PCCP

PAPER

View Article Online
View Journal

Cite this: DOI: 10.1039/d4cp04515g

Nanostructured bismuth ferrite nanoparticles: synthesis, characterization, electrical/magnetic properties and photocatalytic performance

M. H. Ghozza,[a] Ahmed T. Mosleh,[b] Elbadawy A. Kamoun,*[cd] Mahmoud Abdel-Aty,[ef] M. Alfiras,[g] Mohamed Hafez Ahmed,[h] Shawkat Alkhazaleh,[i] V. Ganesh,[jk] H. Y. Zahran[jk] and Ibrahim S. Yahia*[jk]

Nanostructured bismuth ferrite ($BiFeO_3$) single-phase nanoparticles with 76.2% crystallinity and 100% perovskite structure were synthesized using a co-precipitation method. The X-ray diffraction pattern confirmed the perovskite structure of BFO, and Rietveld refinement demonstrated the presence of a triclinic structure with the *P*1 space group. The Scherrer and Williamson–Hall equations were used to calculate the crystallite size (63 and 83 nm, respectively) with a grain size of almost 246 nm and an activation energy of 0.53 eV. The accumulation of free charges at interfaces, which correlate with the sample bulk and the interface between the compound and electrode space-charge polarization, was the reason behind the high values of ε'. As the frequency increased up to 1000 Hz, both dielectric constant ε' and dielectric loss ε' fell quickly. In contrast, at high frequencies, the ε' became more frequency-independent, notably when ε' increased with a temperature of up to 423 K. The sample exhibited considerable soft ferromagnetic-like activity due to the acquired nanoscale structure that promotes spin coating in the $BiFeO_3$ antiferromagnetic phase. The significant coercivity 2624.5 Oe provides each materials in permanent magnetic and transformers. Photocatalytic activity of the $BiFeO_3$ nanocomposite under UVA-light irradiation was performed using Congo red dye. The maximum photocatalytic degradation efficiency after 200 min for CR was 66%. The exceptional electrical and magnetic characteristics of nanostructured $BiFeO_3$ provide new possibilities for its use in potential technological applications, *i.e.*, spintronics, data storage microelectronics, and water treatment.

Received 28th November 2024,
Accepted 11th December 2024

DOI: 10.1039/d4cp04515g

rsc.li/pccp

[a] *Basic Science Department, Cairo Higher Institute for Engineering, Computer Science and Management, New Cairo, Egypt*
[b] *Nanotechnology Section, Egyptian Company for Carbon Materials, El-Sheraton/El-Nozha, Cairo 11757, Egypt*
[c] *Department of Chemistry, College of Science, King Faisal University, Al-Ahsa 31982, Saudi Arabia. E-mail: ekamoun@kfu.edu.sa, badawykamoun@yahoo.com; Tel: +966 201283320302*
[d] *Polymeric Materials Research Dep., Advanced Technology and New Materials Research Institute (ATNMRI), City of Scientific Research and Technological Applications (SRTA-City), New Borg Al-Arab City 21934, Alexandria, Egypt*
[e] *Deanship of Graduate Studies and Research, Ahlia University, PO Box 10878, Manama, Kingdom of Bahrain*
[f] *Jadara Research Center, Jadara University, PO Box 733, Irbid, Jordan*
[g] *Electrical and Electronic Engineering Department, College of Engineering, Gulf University, Sanad 26489, Kingdom of Bahrain*
[h] *Faculty of Engineering and Quantity Surviving, INTI International University Colleges, Nilai, Malaysia*
[i] *Department of Mathematics, Faculty of Sciences, Jadara University, Jordan*
[j] *Central Labs, King Khalid University, P.O. Box 960, AlQura'a, Abha, Saudi Arabia. E-mail: dr_isyahia@yahoo.com, isyahia@gmail.com, ihussein@kku.edu.sa; Tel: +966-593604010*
[k] *Laboratory of Nano-Smart Materials for Science and Technology (LNSMST), Department of Physics, Faculty of Science, King Khalid University, PO Box 9004, Abha 61413, Saudi Arabia*

1. Introduction

One of the most researched multiferroic magneto-electric compounds is bismuth ferrite ($BiFeO_3$, BFO). It reveals the coexistence of magnetic and ferroelectric orders at ambient temperature, where ferroelectricity is thought to be driven by the 6 s lone pair electrons of bismuth. Meanwhile, magnetic ordering results from the partly filled d orbital of the Fe atom. Additionally, BFO is a potential lead-free piezoelectric material with the highest value of remnant polarization (P_r > 100 mC cm^{-2}), according to Baek *et al.* (2011), which makes it appealing for ferroelectric capacitor devices and an extremely high Curie temperature (T_C = 830 °C). As reported, in bulk $BiFeO_3$, three phases are identified: α, β, and γ.[1] Ait Tamerd and his colleagues concluded that BFO comprises two sublattices: the electric dipoles at Bi-sites (the unit cell center) comprise the ferroelectric sublattice. In contrast, the magnetic sublattice involves an anti-ferromagnetic order of Fe-spins and the defect concentration effect on the performance of the device fabricated from BFO.[2]

This ferrite is extensively researched because ferroelectric and magnetic order are coupled at ambient temperature. Numerous useful applications, including ferromagnetic resonance, data storage, sensors, magneto-electric memories, photocatalysts, spintronics, diversity of nanoelectronics, and photovoltaic facilities, are made possible by these material groups' intriguing physical characteristics.[3–10]

These potential materials exhibit single-phase multiferroic behavior based on experimental and theoretical investigation. Recently, a lot of research has been done on these materials. However, bismuth ferrite has a more favorable viewpoint because of its special multifunctional qualities. Since co-precipitation can quickly and affordably manufacture homogeneous nanosized particles, it is a more suited method. Because of bismuth's low evaporation temperature, the preparation of bismuth ferrite is challenging. As a result, secondary phases of bismuth ferrite are produced alongside the primary phase. Synthesis can resolve this issue using the co-precipitation method, although the reaction forbids the development of secondary phases. Recently, the co-precipitation approach has been used to produce BFO nanoparticles. Although they could regulate many processing parameters for the synthesis of BFO, the impure phases could not be eliminated.[11]

Two factors prevented $BiFeO_3$ from being used in novel applications: its small resistivity and significant loss factor due to oxygen non-stoichiometry and its weak magnetism, which is antiferromagnetic below T_N.[11,12] The secondary phases through BFO synthesis and the volatile nature of Bi at high sintering temperatures hinder the practical use of BFO in the industry. The primary sources of leakage current that impact BFO conductivity are the transformation of Fe^{3+} into Fe^{2+} and the formation of oxygen vacancies. Establishing superior multiferroic order in BFO is challenging because of impurity phases such as $Bi_{25}FeO_{39}$ and $Bi_2Fe_4O_9$.[7]

Oxide composition, which establishes their phase stability and physicochemical characteristics, is greatly influenced by oxygen stoichiometry. A deformed triclinic perovskite structure and a *P*1 space group display G-type antiferromagnetic ordering below the Neel temperature (T_N = 370 °C) and ferroelectricity below the Curie temperature ($T_C \approx$ 830 °C). Since both transitions occur above room temperature, magnetoelectric (ME) applications might be possible for both.[4] $BiFeO_3$ is one such material possessing both multiferroic and magnetoelectric capabilities, despite all multiferroic materials lacking magnetoelectric features and *vice versa*. $BiFeO_3$ has a distorted ABO_3-type perovskite structure, because it is ferroelectric lower 830 °C and antiferromagnetic lower 370 °C and due to the secondary phase development, $BiFeO_3$ has limited industrial applicability.

Additionally, when metal doping is done, it is known that oxygen vacancies might increase magnetism. $Bi_{0.6}Sr_{0.4}FeO_{3-\delta}$ was chosen for the study for this reason as well because there will be two contributions to magnetism.[6] In a brief amount of time, at room temperature, Catalan and Scott prepared pure $BiFeO_3$ using an ultrasonic technique without surfactants. The results revealed the increased purity of the material calcined at 600 °C. They discovered that $BiFeO_3$ is unstable at higher temperatures, leading to the formation of secondary phases, including $Bi_2Fe_4O_9$ and $Bi_{25}FeO_{40}$. However, secondary phases and other related impurities limit the actual application of $BiFeO_3$ due to leakage current issues. This is connected to the intricate dynamics of the Bi_2O_3–Fe_2O_3 phase diagram: at high temperatures for a prolonged period, the production of stable compounds, including $Bi_2Fe_4O_9$ and $Bi_{25}FeO_{40}$, takes precedence, while the loss of Bi_2O_3 prevents the $BiFeO_3$ phase from forming. Various wet chemical techniques, including sol–gel, hydrothermal, microwave-assisted hydrothermal, and electrospinning processes, were used to overcome these challenges to prepare high-purity $BiFeO_3$. Specifically, many authors claim that the ultrasonic manufacturing process can produce a pure $BiFeO_3$ phase.[5]

Eliminating organic contaminants from wastewater represents a noteworthy aspect of environmental conservation. Using bleaches, additional marketable pigments, and various toxic dyes has brought attention to environmental remediation initiatives.[13] One of the primary classes of organic compounds, dye components, have a variety of advantageous applications in daily life. For instance, up to 80% of all dyes come from the leather, paper, plastic, and textile industries. The primary category of global water pollutants comprises synthetic dye compounds and other dyestuffs. Ultimately, between 1 and 15% of synthetic fabric colors used in various manufacturing end up in wastewater channels and major water streams.[14,15] A common synthetic anionic dye used as a photosensitizer to color hair, paper, and clothing is called Congo red (CR). CR is a carcinogenic or extremely hazardous dye, even at low doses, according to toxicological assessment.[16] It is difficult to remove dyes from wastewater completely.

Recently, photodegradation of wastewater utilizing nanostructured semiconductors has been demonstrated to be possible with solar energy.[17,18] Many techniques, including adsorption, have been suggested to get rid of this harmful dye,[19] advanced oxidation, photocatalysis,[20] and biodegradation.[21] Photocatalysis is a popular choice among them since it provides a dye treatment procedure that is safe, economical, effective, and eco-friendly. Because of the phase's relatively small temperature stability range, it isn't easy to synthesize bulk BFO in its single-phase and stoichiometric forms. Furthermore, it is challenging to regulate the sample's oxygen stoichiometry because magnetic defect ions, contamination phases (*e.g.*, $Bi_{25}FeO_{39}$, Bi_2O_3, and $Bi_2Fe_4O_9$), and variations from the ideal oxygen stoichiometry are always visible.[22] To investigate the structural, electrical, and magnetic characteristics of multiferroic materials and the photodegradation of Congo red dye, $BiFeO_3$ nanostructure was prepared in this work utilizing a co-precipitation method.

Herein, $BiFeO_3$ NPs were synthesized using a co-precipitation method using $Bi_5H_9N_4O_{22}$ as a raw material instead of $BiNO_3$. The precise procedures used during the synthesis were studied to obtain a single phase of nano-$BiFeO_3$ compared to multiphases of bulk $BiFeO_3$ at a low sintering temperature and a reduced sintering time. The structure and electrical and

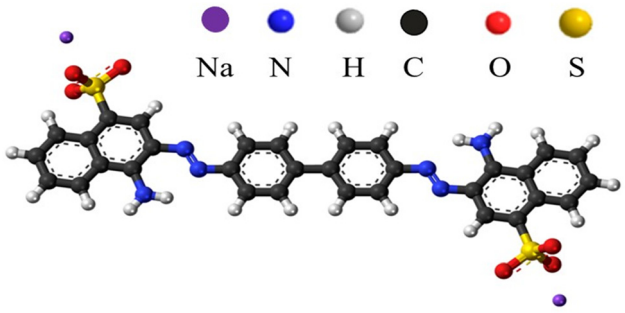

Fig. 1 Structure of Congo red dye.

magnetic properties were explored to introduce such materials in novel applications such as photocatalysts and energy storage applications (Fig. 1).

2. Materials and methods

2.1. Materials

Bismuth subnitrate $Bi_5H_9N_4O_{22}$ (purity 99%, Sigma Aldrich), ferric(III) nitrate $Fe(NO_3)_3{\cdot}9H_2O$ (purity 98%, LOBA chem), nitric acid HNO_3 (purity ≥65.0%, Merck), sodium hydroxide NaOH ((purity ≥97.0%, Merck), Congo red dye $C_{32}H_{22}N_6Na_2O_6S_2$ (purity ≥75.0%, Sigma Aldrich). Sodium chloride (NaCl, purity 98%, LOBA Chem, India), sodium nitrate ($NaNO_3$, purity 98%, LOBA Chem, India), ascorbic acid ($C_6H_8O_6$, purity 99%, Sigma Aldrich, Germany), isopropyl alcohol (C_3H_8O, purity 99%, Alpha Aeser, India), and distilled water (DW) were used.

2.2. Preparation of the BFO nanocomposite

Chemical co-precipitation was employed to prepare $BiFeO_3$ nanoparticles. Stoichiometric amounts of $Bi_5H_9N_4O_{22}$ and $Fe(NO_3)_3{\cdot}9H_2O$ in diluted nitric acid were dissolved in deionized water using a usual process. To make up for the bismuth that disappeared throughout the experiment, an additional 3% bismuth subnitrate was added.[23] After vigorously swirling them together, a transparent solution could be formed. Deionized water and NaOH were used to make a solution of the same volume. Maintaining the solution's pH at 9.3 throughout the operation is important to manage the chemical precipitation process. Two different beakers were filled dropwise and simultaneously with NaOH and metal nitrate solutions while stirring vigorously at 1500 rpm. A brownish colloidal precipitate was generated by mixing liquids. Ultimately, the goods were gathered and repeatedly cleaned with ethanol and distilled water until they achieved a pH of 7. The powder was dried for 3 h at 110 °C before being calcined for 5 hours at 650 °C. The preparation scheme is shown in Fig. 2(a). Eqn (1) shows the chemical equation for the synthesis of BFO NPs:

$$[Bi_5H_9N_4O_{22}] + Fe[(NO_3)_3{\cdot}9H_2O] + n\text{NaOH} \rightarrow BiFeO_3 + n\text{NaCl} + nH_2O \quad (1)$$

2.3. Photocatalytic activity

To study the photocatalytic activity of the $BiFeO_3$ nanocomposite, a photodegradation reaction of dye solution under UVA light irradiation was performed. The photoreactor system was assembled and designed by ECCM Company in Egypt (Fig. 2b). An exceptional wooden box (80 × 70 × 80 cm, $L \times W \times H$) was encased in the photoreactor that uses UVA-visible lamps. The inside is made up of fourteen carefully managed lights, seven of which are ultraviolet-A (UVA) lamps at 367 nm, with a length of 45 cm and an applied power of 18 W, and seven of which are blue-white (BW) lamps at ≥420 nm, with a length of 60 cm and an applied power of 18 W (made by Philips Co., Germany). The merged sample rested in a photoreactor and was exposed to UVA light afterward.[24] First, an aqueous solution of Congo red dye (CR; 10 ppm) was prepared before the addition of the photocatalyst. In a typical photocatalysis reaction, 50 mL of the dye solution was taken in a beaker and mixed with 0.01 g of the catalyst. The prepared solution was stocked in the dark for

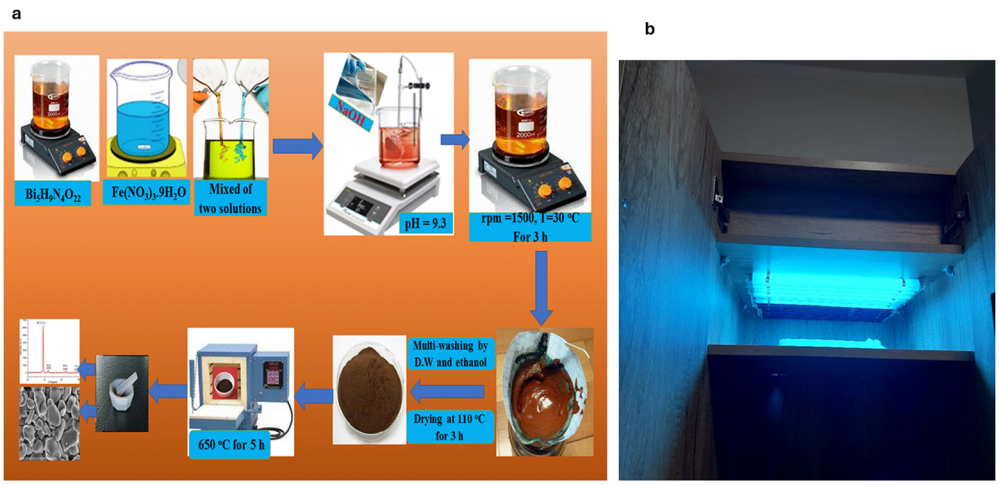

Fig. 2 (a) Scheme of the co-precipitation processes of nano-$BiFeO_3$ and (b) scheme of the used UVA-photoreactor designed by ECCM Company, Egypt.

30 min to fix and reach the adsorption–desorption equilibrium. A UV-visible spectrophotometer was used to observe the degree of degradation of the dye. The degradation efficiency of the dye was computed using the following equation:[25]

$$\text{Degradation efficiency} = \frac{A_0 - A}{A_0} \times 100 \quad (2)$$

where A_0 is the initial absorbance of the dye and A is the absorbance at the chosen time. All absorbance values were determined by maximum absorption at 495 nm for CR dye in the absorption spectrum.

2.4. Characterization of the $BiFeO_3$ nanocomposite

X-ray diffraction (Bruker D8 Discover Germany) measurements were used for testing the powder sample using CuK_α radiation (λ = 1.5415 Å), 40 kV, and 40 mA. The structural parameters were determined by high scores and Rietveld refinement software programs. The morphological and elemental analyses of the synthesized samples were performed using a SEM model, JEOL JSM-6390, Japan, close fitted with an energy dispersive spectroscopy (EDS) system at a voltage of 20 kV and with different resolutions of 3 μm, 1 μm, and 500 nm. The average particle size was calculated using the ImageJ software program. The magnetization measurements were performed at ambient temperature using a Lake Shore VSM7410 vibrating sample magnetometer with a field range of ±20 kOe. The powder is ground well in an agate mortar for half an hour and pressed in a die as a pellet with 13 mm diameter and 2 mm thickness at 300 bar pressure. The electrical resistance (R) is measured using a homemade electrometer from room temperature to 150 °C. DC conductivity (σ) is measured using the traditional equation $\sigma = L/RA$, where L is the thickness and A is the cross-section area.

Dielectric measurements were performed with a dielectric broadband spectrometer in the 1 Hz–100 kHz frequency range at ambient temperature from 25 to 150 °C with a temperature step of 5 °C. A JASCO UV-Vis single beam spectrophotometer was operated to track the photodegradation process under room conditions.

3. Results and discussion

3.1. Structural perspective

X-ray diffraction patterns of $BiFeO_3$ are shown in Fig. 3(a). $BiFeO_3$ was generally observed to be in a rhombohedral phase with the space group $R3c$. However, the crystal structure is indexed *via* the Foolproof refinement software program in the present experiment. The triclinic system structure (space group: $P1$) was claimed to be the most stable.[26] The triclinic $P1$ phase standard data (JCPDS # 01-072-2112) and Bragg angles 2θ of $BiFeO_3$ are similar. No secondary phases are displayed, reflecting the structure's high purity. The predominant peak at the (110) planes of $BiFeO_3$ corresponds to the peak at 32.9°. Thus, a drop in crystallite size and increasing the lattice strain are responsible for the peak's broadening.[27] The Debye–Scherrer formula was used to determine the crystallite size (D),[28] as given in eqn (3).

$$D = \frac{k\lambda}{\beta_D \cos\theta}, \quad (3)$$

where λ is the occurrence radiation wavelength (1.5415 Å), β_D is the full-width at half-maximum in radians, θ is the angle of diffraction, and D is the crystallite size of the most intense peak. The shape factor (k) = 0.89 is also included. The Scherrer equation yields a crystallite size of 62.8 nm. Additional parameters determined for XRD are the degree of crystallinity for the produced matrix (X_c), the microstrain (ε), and the dislocation density (δ).

The solid black line represents the estimated pattern; the red symbols characterize the experimental data. The solid blue

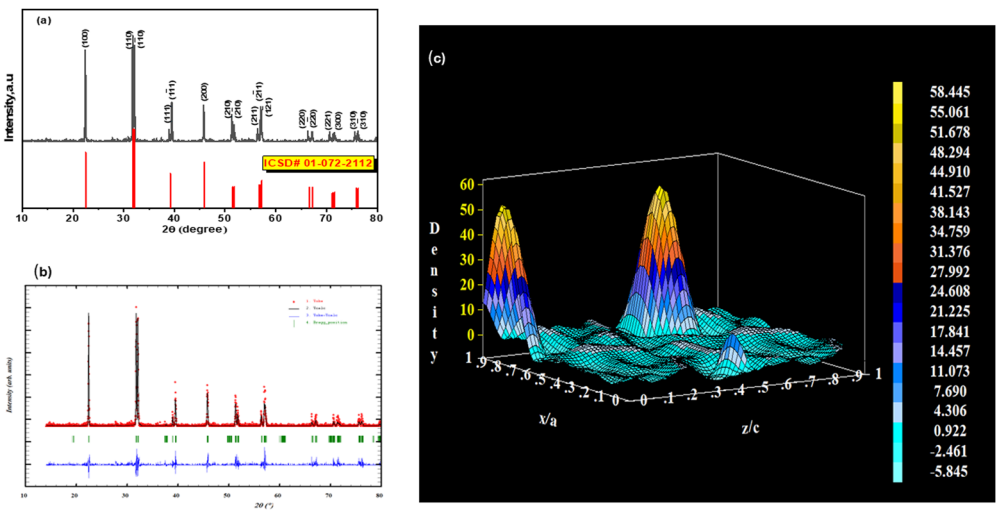

Fig. 3 (a) X-ray diffraction patterns of $BiFeO_3$ and (b) Rietveld refinement patterns of $BiFeO_3$. The red symbols represent the experimental data, whereas the calculated pattern is a solid black line. The difference pattern between the calculated and experimental data is a blue solid line. Blue vertical bars represent Bragg peak positions for their respective crystal structures, and (c) the electron density distribution is achieved using Fourier transformation.

line represents the pattern of discrepancy between the experimental and computed data. For each of their crystal forms, Bragg peak positions are shown by blue vertical bars. A solid blue line represents the pattern of disagreement between the computed and experimental data. Blue vertical bars indicate Bragg peak positions for each of their crystal forms.[29–31]

$$\beta_w = \beta_D + \beta_\varepsilon, \quad (4)$$

which might be represented as follows:

$$\beta_w = \frac{k\lambda}{D \cdot \cos\theta} + 4\varepsilon \tan\theta, \quad (5)$$

Lastly, after being rearranged, it is presented as[32]

$$\beta \cdot \cos\theta = \frac{k\lambda}{D} + 4\varepsilon \sin\theta, \quad (6)$$

One may calculate the dislocation density using the power two reciprocal of the crystallite size.[33]

$$\delta \text{ (dislocation density)} = \frac{1}{D^2}, \quad (7)$$

Here, it is confirmed that the straight-line and previously obtained equations are strikingly similar. The grasped microstrain is shown by the slope of the line (slope = 4ε). On the other hand, the crystallite size is confirmed by the clear intersection of the line with the vertical y-axis. This relationship, known as the Williamson–Hall relation, exists between $\beta \cos\theta$ and $\sin\theta$.[24] Fig. 4a represents the relation matched to a straight line, where the crystallite size is expected to be 82.7 nm and compared with those obtained from Scherrer's equation. The XRD parameters are listed in Table 1. Moreover, the characteristic degree of crystallinity or % perovskite formed (X_c) is derived from the relationship between the area of all peaks (X_{all}) and the area beneath crystalline peaks ($X_{crys.}$) for a completed composite[34,35] reasonably computed with the original software (Fig. 3(b)).

$$x_c = \frac{x_{crys.}}{x_{all}} \times 100, \quad (8)$$

Fig. 3(c) shows Rietveld refinement of $BiFeO_3$ with refined parameter about χ^2 = 1.4 giving lattice parameter values a = 5.5754 (5) Å, b = 5.6320 (8) Å, c = 5.5785 (3) Å, α = 60.31 ± 0.002, β = 59.97 ± 0.004, and γ = 60.35 ± 0.005. These results agree with those reported by Ishrat Naz *et al.*[26] They discovered that, for pure $BiFeO_3$, the bond length of Bi–O is 2.573 Å, and the bond angle of Fe–O–Fe along the [0$\bar{1}$0] direction is 155.13°. Following multiple refinement rounds, $P1$'s final fractional ratios are 100%.

3.2. Microstructural analysis

Fig. 5a and b display the microstructure of $BiFeO_3$ at dissimilar scales 3 μm, 1 μm, 500 nm, and 300 nm. An average particle size of 245.9 nm is obtained when $BiFeO_3$ crystallizes, representing agglomerate particles having unequal axes. The particle size histogram is revealed in Fig. 5b. Fig. 5c, which illustrates the energy dispersive spectroscopy results of $BiFeO_3$, shows the atomic% of elements Bi, Fe, and O as 0.12, 0.39, and 99.48, respectively. The atomic percentages of Bi^{3+} and Fe^{3+} ions are compared, and it appears that the former is less abundant than the latter due to the volatilization of Bi^{3+} ions throughout heat treatment, which is predicted to change the material's electrical and magnetic properties.[36]

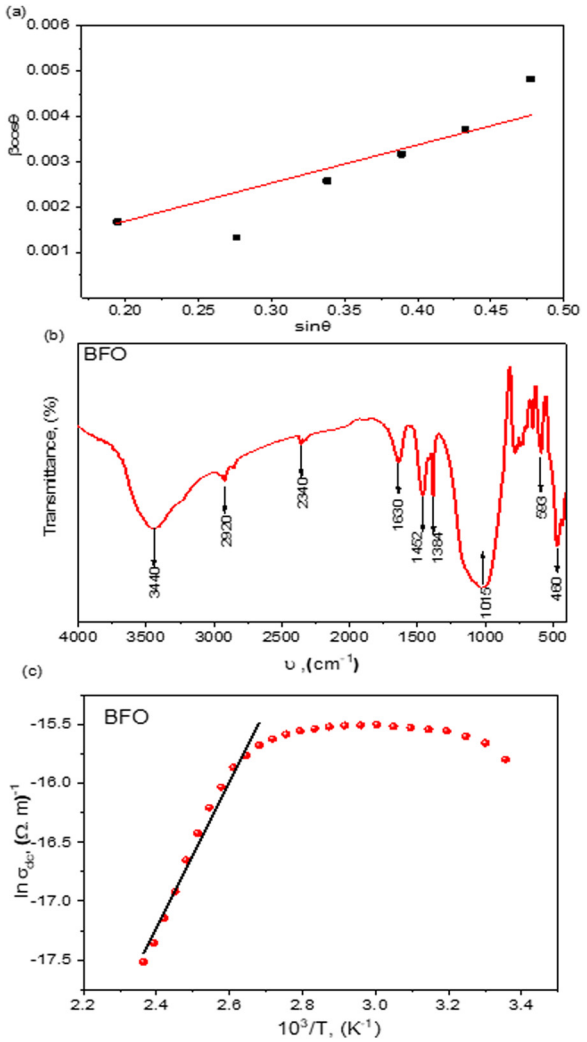

Fig. 4 (a) Williamson–Hall plot with linear fitting parameters of nano-$BiFeO_3$, (b) FTIR spectra of $BiFeO_3$ nanoparticles, and (c) temperature dependence of DC electrical conductivity of nano-$BiFeO_3$.

Table 1 Structural parameters of nano-$BiFeO_3$

I.C.S.D. 01-072-2112	$BiFeO_3$
%Crystallinity	76.2
%Perovskite	100
Crystallite size Scherrer	62.8
Crystallite size, nm (W–H)	82.7
Grain size, nm	245.9
Strain $\varepsilon \times 10^{-3}$	2.07
Dislocation density $\times 10^{-4}$, nm^2	2.5
V, Å^3	124.45

3.3. FT-IR analysis

FT-IR spectra of produced BFO nanoparticles at the ν 400–4000 cm^{-1} region are shown in Fig. 4b. The formation of a

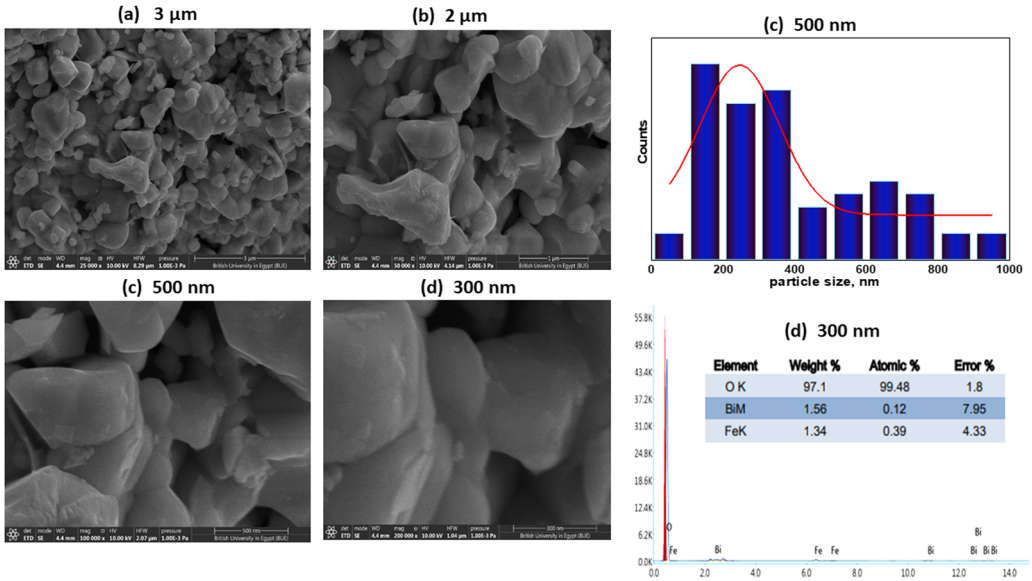

Fig. 5 (a)–(c) SEM of $BiFeO_3$ at different magnifications, (d) histogram of particle size, and (e) EDX and percentage of elements.

perovskite structure is verified by FT-IR analysis. Because of strong bonding, metal-containing nitrogen and oxygen vibrations typically occur in the infrared spectrum below ν 600 cm^{-1}, meaning that they are typically found in high energy ranges.[11] O–Fe–O bending vibrations and Fe–O tensile vibrations associated with FeO_6 groups in the perovskite compounds are represented by two peaks at ν 556.10 and 449.58 cm^{-1}.[37] The band corresponding to O–H vibrations is seen at ν 3444.78 cm^{-1}. NH vibrations can be seen in the same region, although they may overlap with the O–H band because of widening. Nitrate tensile vibrations have also been reported at the ν 1060–1162 cm^{-1} range.[38]

3.4. Temperature dependence on DC electrical conductivity

It was discovered that the conductivity of $BiFeO_3$ showed a linear trend with temperature, suggesting a thermally activated transport mechanism.[39] The Arrhenius relationship can be used to calculate the activation energy.[39] An Arrhenius-type equation was used to fit the portion of the curve to determine the activation energy needed to start conduction:[40]

$$\sigma_{DC} = \sigma_0 e^{\frac{-E_a}{k_B T}}, \quad (9)$$

where T is the temperature, k_B is Boltzmann's constant (k_B = 8.617 × 10^{-5} eV K^{-1}), E_a is the activation energy, and σ_{DC} is a pre-exponential factor. The change of σ_{DC} *versus* $10^3/T$ is shown in Fig. 4c. Based on the conductivity and modulus spectra, the activation energy values are 0.53 eV. Notably, the activation energy value is consistent with the literature and is in the same order of magnitude as other materials based on iron.[41,42] The activation energy of $BiFeO_3$ was determined by fitting the curve depicted in Fig. 4c.

3.5. Frequency and temperature dependence of AC conductivity

Under controlled temperature variations between 298 and 423 K, $BiFeO_3$ orthoferrite's dielectric characteristics and AC conductivity were measured in the frequency range of 1 Hz–100 kHz. The sample impedance Z, sample capacitance C_p, and loss tangent tan δ were measured directly using a programmable automatic HIOKI 3522-50 L.C.R. HiTester meter. Every capacitance C_p value that was extracted from the bridge screen was parallel to the resistance R. Using the following equation, the total conductivity $\sigma_t(\omega)$ was determined:[22]

$$\sigma_T(\omega) = \frac{d}{AZ}, \quad (10)$$

where A is the sample cross-sectional area and d is the sample thickness. The relationship was used to compute the AC conductivity, $\sigma_{AC}(\omega)$:[23]

$$\sigma_{AC}(\omega) = \sigma_T(\omega) - \sigma_{DC}(0), \quad (11)$$

where $\sigma_{DC}(0)$ is termed as the DC conductivity. According to eqn (9), Fig. 6(a) and (b) depict the variation of $\sigma_{AC}(\omega)$ with the temperature between 298 and 423 K and frequency between 1 and 100 kHz. As the temperature rises, σ_{AC} falls, as shown in Fig. 6a, suggesting that charge carrier hopping has a relatively weak temperature dependence. As seen in Fig. 8b, hopping conduction is the main mechanism; this behavior was covered in a previously published study.[43] Since the frequency's pumping force aids in the movement of charge carriers between the various localized states, conductivity rises with frequency.

3.6. Frequency and temperature dependency of ε' and ε''

Eqn (12) was used to obtain the dielectric constant:

$$\varepsilon' = \frac{C_p d}{A\varepsilon_0}, \quad (12)$$

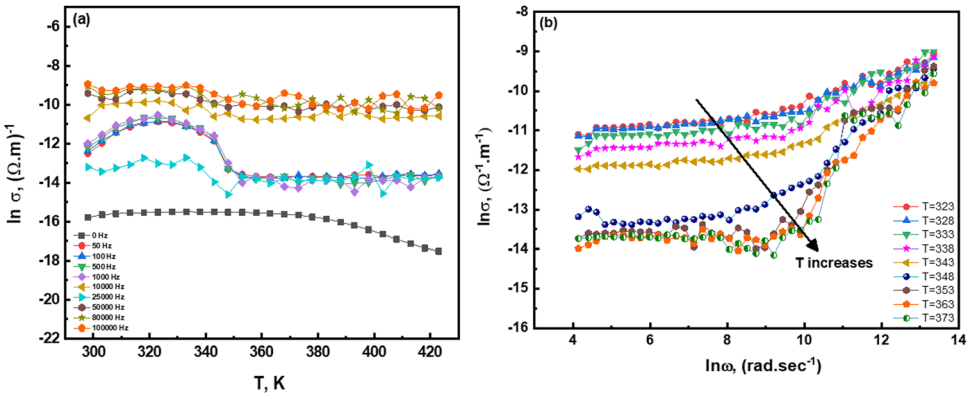

Fig. 6 (a) and (b) Temperature and frequency dependence on AC electrical conductivity of nano-$BiFeO_3$.

where ε_0 is the free space permittivity (8.85×10^{-12} F m^{-1}), A is the sample cross-sectional area (m^2), d is the sample thickness (m), and C_p is the capacity in Farad that was acquired straight from the bridge. Eqn (13) was utilized to compute the dielectric loss ε''.

$$\varepsilon'' = \varepsilon' \times \tan\delta, \tag{13}$$

Fig. 6(a) shows that at higher frequencies, σ_{AC} does not depend significantly on temperature. While for low frequencies, σ_{AC} depends on temperature. The σ_{AC} increases with increasing temperature from RT to 333 K and decreases again beyond $T = 333$ K.

The frequency-dependence of dielectric constant ε' at various temperatures is displayed in Fig. 7(a) and (b). Similar dielectric constant behavior was seen in other literature studies that were examined.[44,45] The figure demonstrates that ε' rises with temperature and falls with frequency. Since ε' for polar materials is mostly described at low frequencies by the multi-component of polarizability, deformational (ionic and electronic) and relaxational (orientational and interfacial) polarization, the reduction of ε' with frequency can be explained naturally.[43] Initially, displacement of the valence electrons, considering the positive nucleus, causes electrical polarization. The frequencies at which this kind of polarization occurs are as high as 10^{16} Hz. Ionic polarization, the second kind, is brought about by the displacement of positive and negative ions. Ionic polarization reaches its highest frequency at 10^{13} Hz. Third, if the material has molecules with a permanent electric dipole moment that may shift their orientation in the direction of an applied electric field, dipolar polarization will occur. Dipolar polarization occurs at up to 10^{10} Hz in frequency. The last one is space charge polarization, which is brought on by interfaces that impede mobile charge carriers. The usual frequency range for space charge polarization is 1–10^3 Hz. The sum of these four polarization kinds can be used to determine the dielectric material's overall polarization.[46] Total polarization is a term that can be used to describe the findings of this investigation. Since orientational polarization takes longer than electronic and ionic polarization, it diminishes as the frequency increases. As a result, interfacial polarization-corresponding values of the dielectric constant fall and eventually reach a constant value at higher frequencies.

Ahmed *et al.*[47] illustrated how a drop in ε' at high frequencies causes the friction between the dipoles to grow, which in turn increases the amount of heat created and disturbs the alignment of the dipoles. On the other side, the figure indicates that ε' rises as the temperature does. Dipoles cannot orient themselves at low temperatures due to orientational polarization associated with the thermal motion of molecules, which is responsible for the temperature-dependent increase of ε'. The dielectric constant ε' increases with temperature because an increase in temperature facilitates the dipole's orientation and raises the value of orientational polarization. The rise in the

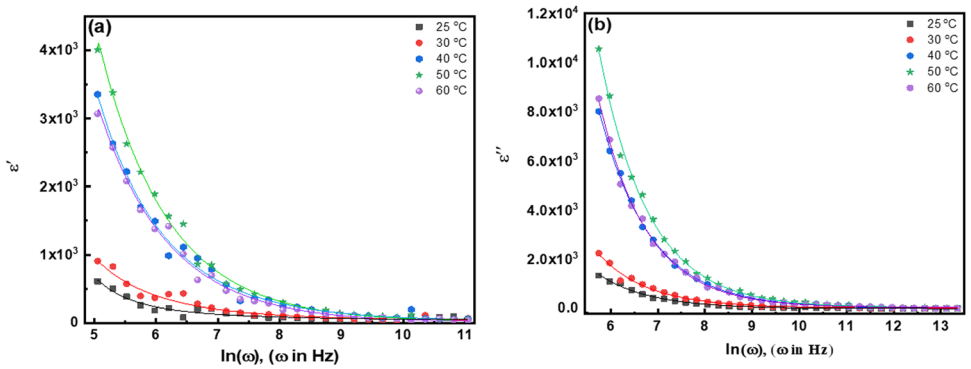

Fig. 7 (a) and (b) Frequency dependence of ε' and ε'' of nano-$BiFeO_3$.

degree of crystallinity is also the cause of the increase in ε'. M. A. Ahmed *et al.* also[47] clarify that to release the localized dipoles to be orientated in the direction of the field, decreasing ε' in low-temperature regions to the thermal energy applied to the samples was not enough. On the other hand, thermal energy frees other localized dipoles at high temperatures, and the field attempts to align them in its direction by rotational or orientational motion, which increases ε'.

Fig. 7(b) illustrates how the dielectric loss ε'' varies with frequency at various temperatures. The magnitude of the dielectric loss increases as the temperature rises. Three components comprise the dielectric loss: vibrational, dipole, and conduction losses. Large-scale ion movement is likely involved in the loss attributable to conduction. This motion is identical to that which happens when direct current is conducted. The ions transcend the network's maximum potential. Heat is transferred from the moving ions to the lattice in proportion to σ_{AC}, and this heat loss occurs once every cycle. Conduction losses are at their lowest at low temperatures, whereas they rise with temperature because $\sigma_{AC}(\omega)$ increases with temperature. As a result, the value of ε'' increases with temperature. Dipole polarization originates from the increase in dielectric loss at low frequencies.

Conversely, ε'' diminishes as frequency increases within the examined range. Since the main reason for the dielectric loss ε'' at low frequencies is ion migration, the reduction of ε'' with frequency may be explained. As a result, in addition to ion polarization, ε'' at low and intermediate frequencies is exemplified by great values of ε'' because of the contributions of ion jump and conduction loss of ion migration. However, ε'' diminishes at higher frequency values because ion vibrations can be the only source of dielectric loss at such frequencies. The hopping theory of charge carriers over a potential obstruction between charged defects can be utilized to examine the acquired ε'' data.[43]

3.7. Magnetic characterization

Fig. 8 shows the *M*–*H* hysteresis loop of $BiFeO_3$ at a range ± 20 kOe at room temperature. The systematic magnetic property has been detected, and the samples show substantial size hysteresis loops, indicating hard ferromagnetic activity and the isotropic crystalline magnetic structure. The magnetization curve does not reach saturation even at a magnetic field of 20 kOe, the maximum magnetization M_s = 0.68351 emu g^{-1}, coercive field H_c = 2624.5 Oe, and remnant magnetization M_r = 0.26314 emu g^{-1}. This result indicates that the perovskite crystalline structure has good magnetic applicability compared to that reported in ref. 48.

This finding is comparable to some reported results elsewhere.[11,45,47,49,50] Pure and rare earth-doped $BiFeO_3$ polycrystalline ceramics are tabulated in Table 2. Significant value M_s of $BiFeO_3$ arises from the good structural and morphological properties, which in turn accompanied the formation of a pure $BiFeO_3$ nanostructured phase. Doga Bilican *et al.*[50] reported that because of the size effects, which cause the spiral spin structure to be suppressed and lead to antiferromagnetic spin

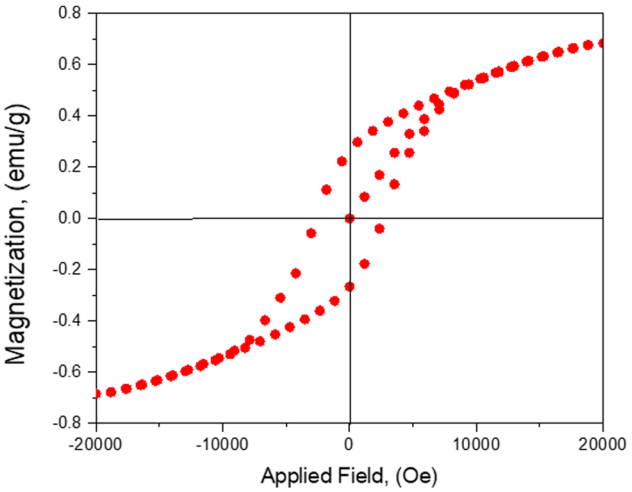

Fig. 8 Magnetization *vs.* magnetic field of nano-$BiFeO_3$.

canting, $BiFeO_3$ may potentially contribute to ferromagnetism. Thus, the main source of the detected ferromagnetic reaction may be the reinforcement of antiferromagnetic spin canting by nanostructuring processes, which results in a greater net magnetism.

Conversely, the great magnitude of coercivity at 650 °C may have to do with forming other paramagnetic phases, which most likely tend to separate the BFO grains. The diminishing dipolar and exchange interactions between granules may harm the coercivity. The average magnetic moment per molecule (μ_{eff}) unit in the Bohr magneton of $BiFeO_3$ is calculated using eqn (14);[47]

$$\mu_{eff} = \frac{M_w \cdot M_s}{5585}, \quad (14)$$

where M_w denotes the sample's molecular weight, and M_s denotes its saturation magnetization.[49] μ_{eff} gives the number of Bohr magnetons (BM) per molecule and is roughly estimated using the above equation to be 0.031 BM. This demonstrates that $BiFeO_3$ has the potential for connecting magnetic and electrical ordering, making it appropriate for use in a magnetic storage medium. On average, the magnetic moment per Fe ion in $BiFeO_3$ is $0.0049\mu_B$ per Fe.[11] With the discrepancy between the significant magnitude of our sample and others ascribed to nanoparticles lesser than approximately 62 nm, the intrinsic spiral spin structure with a period length of $\sim$62 nm is also largely suppressed, resulting in the observed weak magnetism consistent with that reported elsewhere.[54] High concentrations of dislocations in $BiFeO_3$ NPs may be utilized to openly control their magnetic properties because they produce an unusual magnetic behavior that changes the magnetic hysteresis from an antiferromagnetic-like to a weak-ferromagnetic-like loop when high dislocation density and reduced crystallite size are introduced.[55]

3.8. Photocatalysis features

BFO was subjected to photocatalytic measurement to check its efficiency in degrading Congo-red dye (CR). The photocatalytic

Table 2 Some BFO photocatalysts and the effectiveness of organic pollutants' photodegradation

Catalysts	Dyes	Catalyst dose (g)	Dye concentration	Light sources	Time (min)	Degradation efficiency (%)	Rate constant (min^{-1})	Ref.
BFO	CR	0.01	10 ppm	UVA	200	65.7	0.00693	Present work
BFO	CR	—	1 ppm	Hg lamp, 160 W	360	30	—	51
BFO	RhB	0.02	1×10^{-5} M	Visible light	60	—	0.0692	52
BFO	CR	1	10 ppm	Solar light	60	77	—	53

activities of BFO are shown in Fig. 9(a); the degradation efficiency of BFO is 65.5% in 200 min, showing a considerable CR dye removal with BFO. As illustrated in Fig. 9(b), under visible light irradiation, results demonstrate that the degradation reactions often follow a Langmuir–Hinshelwood apparent pseudo-first-order kinetics equation. The kinetic linear simulation curves of the photocatalytic degradation of CR by BFO are shown in Fig. 9(c):[56,57]

$$\ln\left(\frac{A}{A_0}\right) = -kt, \tag{15}$$

where A is the absorbance at the desired time, t is the time, k is the rate constant, and A_0 is the dye's initial absorbance. Fig. 9(c) shows that the apparent first-order rate constant k for BFO was 0.00693 min^{-1}. The following relationship was used to calculate the dye solution's 50% ($T_{1/2}$, or half-life) duration:[58]

$$T_{1/2} = \frac{0.693}{k}, \tag{16}$$

It was found that Congo red dye's half-life value ($T_{1/2}$) for the example BFO is approximately 100 minutes. Fig. 9(c) displays the observation and diagrams related to the rate constant.

3.9. Photocatalytic degradation mechanism of CR dye

Fig. 9(d) illustrates the reactive species that contribute to the degradation of CR. The hydroxyl radicals ($^{\bullet}OH$), superoxide radicals ($O_2^{\bullet-}$), electrons (e^-), and holes (h^+) were captured by isopropanol (IPA), ascorbic acid (ASC), sodium nitrate ($NaNO_3$), and sodium chloride (NaCl), respectively. According to the figure, the degradation rate significantly drops when IPA and ASC are used as trapping agents, demonstrating the critical role that $O_2^{\bullet-}$ radicals play in photodegradation. However, when IPA is used, the activity nearly stays the same as that of $BiFeO_3$ NPs, indicating that the $^{\bullet}OH$ radical affects photocatalytic CR dye degradation.[59] To break down the CR dye, this produces holes (h^+) and electrons (e^-) on the $BiFeO_3$ NP catalytic surface. The production of $^{\bullet}OH$ radicals on the photocatalyst surface, which results from the oxidation of the H_2O molecule, causes the diazo groups in CR dye to be broken down.[60,61] The water molecule on the absorbing hole (h^+) gives $^{\bullet}OH$ radicals, which produce H_2O and CO_2 byproducts beyond reactions. The basic steps in equation form are as follows (eqn (17)–(21)):

$$BiFeO_3 + h\nu \rightarrow BiFeO_3(h^+) + BiFeO_3(e^-) \tag{17}$$

$$O_2 + e^- \rightarrow O_2^{\bullet-} \tag{18}$$

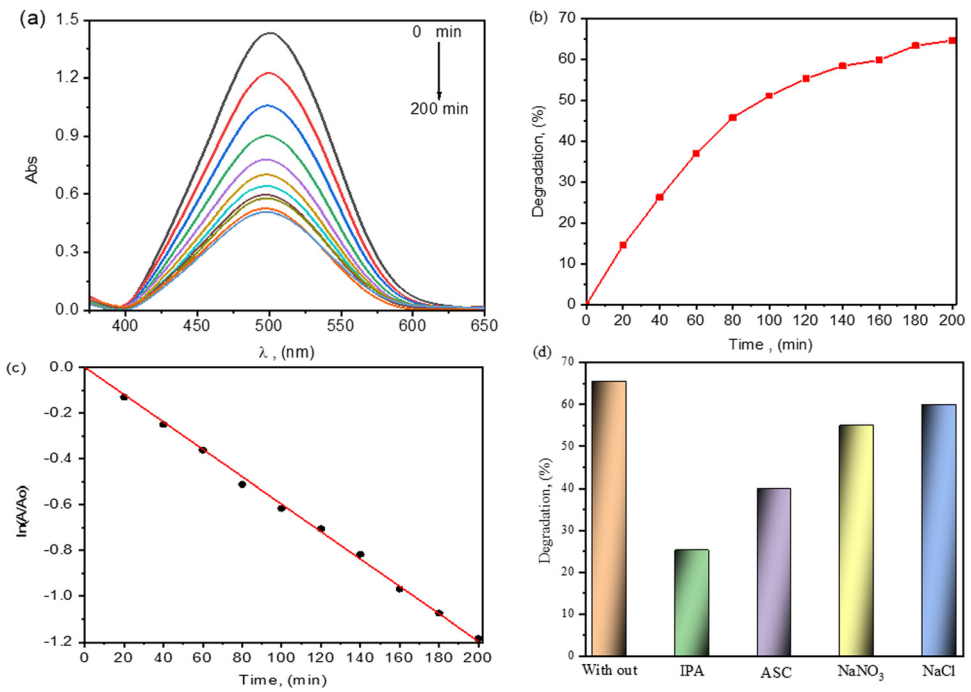

Fig. 9 (a) The absorption spectra of CR solution under visible light irradiation, (b) degradation efficiency, (c) kinetic rate constant, and (d) trapping agent of CR dye with $BiFeO_3$ NPs.

$$h^+(VB) + H_2O \rightarrow H^+ + OH^\bullet \quad (19)$$

$$O_2 + 2H_2O + 2e^-(CB) \rightarrow 2OH^\bullet \quad (20)$$

$$OH^\bullet + O_2^{\bullet -} + \text{CR dye} \rightarrow CO_2 + H_2O \quad (21)$$

4. Conclusions

Using a chemical co-precipitation approach, bismuth ferrite nanoparticles were effectively produced at 650 °C for three hours of calcination. XRD patterns were utilized to implement structural and phase studies. XRD data verify that a crystallite size of 62.8 nm could be produced containing just a pure BFO phase, free of any impurities or secondary phases. Based on the Rietveld refinement of the sample fitted with the Foolproof Program, a triclinic structure with the space group *P*1 was found. The SEM image also demonstrates the regular distribution and average size of the particles (245.9 nm) that comprise bismuth ferrite. With significant dielectric losses, all current samples have dielectric constants in the region of 10^3. These losses are mostly caused by DC conduction in these samples. The Arrhenius curve and the behavior of activation energies suggest that the ionic conduction sample is predominant. Examining the samples' magnetic characteristics reveals that, at room temperature, the nanoparticles behave in a hard ferromagnetic manner. At the same time, it is an antiferromagnetic material with a bulk cycloidal spin structure. The co-precipitation process with sintering temperature is projected to be the ideal condition for obtaining the pure phase of BFO in a form appropriate for the interesting electrical and magnetic issues that would stimulate device applications. After 200 minutes, CR's greatest photocatalytic degradation efficiency was 65.7%, and $^\bullet$OH radical affects photocatalytic CR dye degradation.

Author contributions

M. H. Ghozza and Ahmed T. Mosleh: carried out experimental work, data acquisition, interpretation of data, and data analysis and wrote the original draft; H. Y. Zahran, Mahmoud Abdel-Aty, V. Ganesh, M. H. Ahmed, M. Alfiras, and Shawkat Alkhazaleh: helped with resources, carried out data analysis and partly wrote the original manuscript; and E. A. Kamoun and I. S. Yahia: design of the work, draft revision, and revision of the final draft. All authors have critically reviewed and approved the final draft and are responsible for the content and similarity index of the manuscript.

Compliance with ethical standards

Not applicable; no animal was used in this study.

Data availability

The datasets used and analyzed during the current study are available from the corresponding authors (E. A. Kamoun and I. S. Yahia) on reasonable request.

Conflicts of interest

The authors declare that they have no competing interests.

Acknowledgements

The authors extend their appreciation to the University Higher Education Fund for funding this research work under the Research Support Program for Central Labs at King Khalid University through project number CL/PAT/9.

References

1 H. Wang, C. Yang, J. Lu, M. Wu, J. Su, K. Li, J. Zhang, G. Li, T. Jin and T. J. I. C. Kamiyama, On the Structure of α-$BiFeO_3$, *Inorg. Chem.*, 2013, **52**(5), 2388–2392.
2 M. A. Tamerd, B. Abraime, A. Kadiri, A. Lahmar, M. El Marssi, M. Hamedoun, A. Benyoussef and A. El Kenz, Prediction of magnetoelectric properties of defect $BiFeO_3$ thin films using Monte Carlo simulations, *J. Magn. Magn. Mater.*, 2021, **539**, 168402.
3 D. O. Alikin, A. P. Turygin, J. Walker, A. Bencan, B. Malic, T. Rojac, V. Y. Shur and A. L. Kholkin, The effect of phase assemblages, grain boundaries and domain structure on the local switching behavior of rare-earth modified bismuth ferrite ceramics, *Acta Mater.*, 2017, **125**, 265–273.
4 K. Remya, D. Prabhu, R. J. Joseyphus, A. C. Bose, C. Viswanathan and N. Ponpandian, Tailoring the morphology and size of perovskite $BiFeO_3$ nanostructures for enhanced magnetic and electrical properties, *Mater. Des.*, 2020, **192**, 108694.
5 R. Yuansheng, Y. Hong and H. Zhi, Modification of eutectic silicon and β-Al5FeSi phases in as-cast ADC12 alloys by using samarium addition, *J. Rare Earths*, 2013, **31**(9), 916–922.
6 G. Catalan and J. F. Scott, Physics and applications of bismuth ferrite, *Adv. Mater.*, 2009, **21**(24), 2463–2485.
7 F. Ullah, M. Awan, Z. Wazir, I. Sabir and A. ul Haq, Effect of Heat Treatment and La doping on the electrical properties of $BiFeO_3$, *J. Chem. Soc. Pak.*, 2018, **40**(05), 886.
8 W. Mohamed and A. M. Abu-Dief, Impact of rare earth europium (RE-Eu^{3+}) ions substitution on microstructural, optical and magnetic properties of $CoFe_{2-x}Eu_xO_4$ nanosystems, *Ceram. Int.*, 2020, **46**(10), 16196–16209.
9 W. Mohamed, A. Nucara, G. Calestani, F. Mezzadri, E. Gilioli, F. Capitani, P. Postorino and P. Calvani, Optical study of the vibrational and dielectric properties of $BiMnO_3$, *Phys. Rev. B: Condens. Matter Mater. Phys.*, 2015, **92**(5), 054306.

10 W. Mohamed, M. Alzaid, M. SM Abdelbaky, Z. Amghouz, S. García-Granda and A. M. Abu-Dief, Impact of Co^{2+} substitution on microstructure and magnetic properties of $Co_xZn_{1-x}Fe_2O_4$ nanoparticles, *Nanomaterials*, 2019, **9**(11), 1602.

11 H. Maleki, M. Haselpour and R. Fathi, The effect of calcination conditions on structural and magnetic behavior of bismuth ferrite synthesized by co-precipitation method, *J. Mater. Sci.: Mater. Electron.*, 2018, **29**, 4320–4326.

12 X. Qi, J. Dho, R. Tomov, M. G. Blamire and J. L. MacManus-Driscoll, Greatly reduced leakage current and conduction mechanism in aliovalent-ion-doped $BiFeO_3$, *Appl. Phys.*, 2005, **86**(6), 062903.

13 H. Zhu, R. Jiang, L. Xiao, Y. Chang, Y. Guan, X. Li and G. Zeng, Photocatalytic decolorization and degradation of Congo Red on innovative crosslinked chitosan/nano-CdS composite catalyst under visible light irradiation, *J. Hazard.*, 2009, **169**(1–3), 933–940.

14 M. Bilal, T. Rasheed, Y. Zhao and H. M. Iqbal, Agarose-chitosan hydrogel-immobilized horseradish peroxidase with sustainable bio-catalytic and dye degradation properties, *Int. J. Biol. Macromol.*, 2019, **124**, 742–749.

15 M. Salazar-López, M. D. J. Rostro-Alanis, C. Castillo-Zacarías, A. L. Parra-Guardado, C. Hernández-Luna, H. M. Iqbal and R. Parra-Saldivar, Induced degradation of anthraquinone-based dye by laccase produced from Pycnoporus sanguineus (CS43), *Water, Air, Soil Pollut.*, 2017, **228**, 1–10.

16 J. D. Sosa-Martínez, N. Balagurusamy, J. Montañez, R. A. Peralta, R. D. F. P. M. Moreira, A. Bracht, R. M. Peralta and L. Morales-Oyervides, Synthetic dyes biodegradation by fungal ligninolytic enzymes: Process optimization, metabolites evaluation and toxicity assessment, *J. Hazard. Mater.*, 2020, **400**, 123254.

17 Y. Zhang, J. Lu, M. R. Hoffmann, Q. Wang, Y. Cong, Q. Wang and H. J. R. A. Jin, Synthesis of $gC_3N_4/Bi_2O_3/TiO_2$ composite nanotubes: enhanced activity under visible light irradiation and improved photoelectrochemical activity, *RSC Adv.*, 2015, **5**(60), 48983–48991.

18 S. Hernández, D. Hidalgo, A. Sacco, A. Chiodoni, A. Lamberti, V. Cauda, E. Tresso and G. Saracco, Comparison of photocatalytic and transport properties of TiO 2 and ZnO nanostructures for solar-driven water splitting, *Phys. Chem. Chem. Phys.*, 2015, **17**(12), 7775–7786.

19 S. Singh, S. Perween and A. Ranjan, Dramatic enhancement in adsorption of congo red dye in polymer-nanoparticle composite of polyaniline-zinc titanate, *J. Environ. Chem. Eng.*, 2021, **9**(3), 105149.

20 C. M. Magdalane, G. M. A. Priyadharsini, K. Kaviyarasu, A. I. Jothi and G. G. Simiyon, Synthesis and characterization of TiO_2 doped cobalt ferrite nanoparticles *via* microwave method: Investigation of photocatalytic performance of congo red degradation dye, *Surf. Interfaces*, 2021, **25**, 101296.

21 K. L. Maurya, G. Swain, R. K. Sonwani, A. Verma and R. S. Singh, Biodegradation of Congo red dye using polyurethane foam-based biocarrier combined with activated carbon and sodium alginate: Batch and continuous study, *Bioresour. Technol.*, 2022, **351**, 126999.

22 D. Varshney, A. Kumar and K. Verma, Effect of A site and B site doping on structural, thermal, and dielectric properties of $BiFeO_3$ ceramics, *J. Alloys Compd.*, 2011, **509**(33), 8421–8426.

23 B. Cullity and S. Stock, *Elements of X-ray diffraction prentice hall upper saddle river*, NJ, 3rd edn, 2001.

24 A. T. Mosleh, E. A. Kamoun, S. H. El-Moslamy, S. A. Salim, H. Y. Zahran, S. H. Zyoud and I. S. Yahia, Performance of Ag-doped CuO nanoparticles for photocatalytic activity applications: Synthesis, characterization, and antimicrobial activity, *Discover Nano*, 2024, **19**(1), 166.

25 L. Hu, M. Li, L. Cheng, B. Jiang and J. Ai, Solvothermal synthesis of octahedral and magnetic $CoFe_2O_4$-reduced graphene oxide hybrids and their photo-Fenton-like behavior under visible-light irradiation, *RSC Adv.*, 2021, **11**, 22250.

26 I. Naz, F. Ahmad, B. U. Haq, H. Anwar, I. Khadka, M. Alsardia and S.-H. Kim, First-principles calculations to investigate the electronic and optical properties of hexagonal, triclinic, and monoclinic structures of α-$BiFeO_3$, *Mater. Sci. Eng., B*, 2022, **284**, 115838.

27 K. Wan, J. Yang, D. Wang and X. Wang, Graphene oxide@3D hierarchical SnO_2 nanofiber/nanosheets nanocomposites for highly sensitive and low-temperature formaldehyde detection, *Molecules*, 2019, **25**(1), 35.

28 H. Yan, Z. Chen, L. Zeng, Z. Wang, G. Zheng and R. Zhou, The effect of rGO-doping on the performance of SnO_2/rGO flexible humidity sensor, *Nanomaterials*, 2021, **11**(12), 3368.

29 A. M. El Nahrawy, A. Elzwawy, M. Alam, B. A. Hemdan, A. M. Asiri, M. R. Karim, A. B. Abou Hammad and M. M. Rahman, Synthesis, structural analysis, electrochemical and antimicrobial activities of copper magnesium zirconosilicate ($Cu_{20}Mg_{10}Si_{40}Zr$ (30−x) O:(x = 0, 5, 7, 10) Ni^{2+}) nanocrystals, *Microchem. J.*, 2021, **163**, 105881.

30 V. Mote, Y. Purushotham and B. Dole, Williamson-Hall analysis in estimation of lattice strain in nanometer-sized ZnO particles, *J. Theor. Appl. Phys.*, 2012, **6**, 1–8.

31 M. Morsy, A. Darwish, M. Mokhtar, Y. Elbashar and A. Elzwawy, Preparation, investigation, and temperature sensing application of rGO/SnO_2/Co_3O_4 composite, *J. Mater. Sci.: Mater. Electron.*, 2022, 1–15.

32 O. El-Sayed, M. Ghozza and R. A. E. Hamid, Structure, electrical, and optical properties of $Co_{0.7-x}Zn_xNi_{0.3}Fe_2O_4$ ($0.3 \geq x \geq 0.7$) nano-ferrite by sol–gel auto-combustion technique, *J. Aust. Ceram. Soc.*, 2024, 1–14.

33 A. M. El Nahrawy, A. Elzwawy, A. B. Abou Hammad and A. Mansour, Influence of NiO on structural, optical, and magnetic properties of Al_2O_3–P_2O_5–Na_2O magnetic porous nanocomposites nucleated by SiO_2, *Solid State Sci.*, 2020, **108**, 106454.

34 E. Ouda, A. Elzwawy and E.-S. M. Duraia, A facile microwave irradiation synthesis of GO/CNTs hybrids doped with MnO_2: structural and magnetic analysis, *Appl. Phys. A: Mater. Sci. Process.*, 2021, **127**(9), 676.

35 S. Chootin and T. Bongkarn, Optimum conditions for preparation of high-performance $(Ba_{0.97}Ca_{0.03})(Ti_{0.94}Sn_{0.06})O_3$

ceramics by solid-state combustion, *J. Electron. Mater.*, 2017, **46**, 5215–5224.
36 R. Rajesh and S. J. Ethilton, K. Ramachandran, K. Ramesh Kumar, Samba Siva Vadla & IB Shameem Banu, *Appl. Phys. A: Mater. Sci. Process.*, 2018, **124**, 1–9.
37 J.-H. Xu, H. Ke, D.-C. Jia, W. Wang and Y. Zhou, Low-temperature synthesis of $BiFeO_3$ nanopowders *via* a sol–gel method, *J. Alloys Compd.*, 2009, **472**(1–2), 473–477.
38 S. Zhang, M. Lu, D. Wu, Y. Chen and N. Ming, Larger polarization and weak ferromagnetism in quenched $BiFeO_3$ ceramics with a distorted rhombohedral crystal structure, *Appl. Phys. Lett.*, 2005, **87**(26), 262907.
39 A. Omri, M. Bejar, E. Dhahri, M. Es-Souni, M. Valente, M. Graça and L. Costa, Electrical conductivity and dielectric analysis of $La_{0.75}(Ca,Sr)_{0.25}Mn_{0.85}Ga_{0.15}O_3$ perovskite compound, *J. Alloys Compd.*, 2012, **536**, 173–178.
40 M. Ghozza and I. S. Yahia, Impact of gadolinium doping on structure, electrical and magnetic properties of Gd_xCd_{1-x}-MnO_3 manganite nanoparticles, *J. Mater. Sci.: Mater. Electron.*, 2021, **32**(9), 11628–11639.
41 N. Chihaoui, R. Dhahri, M. Bejar, E. Dharhi, L. Costa and M. Graça, Electrical and dielectric properties of the $Ca_2MnO_{4-\delta}$ system, *Solid State Commun.*, 2011, **151**(19), 1331–1335.
42 A. Dhahri, F. Rhouma, J. Dhahri, E. Dhahri and M. Valente, Structural and electrical characteristics of rare earth simple perovskite oxide $La_{0.57}Nd_{0.1}Pb_{0.33}Mn_{0.8}Ti_{0.2}O_3$, *Solid State Commun.*, 2011, **151**(9), 738–742.
43 H. El-Mallah, AC Electrical Conductivity and Dielectric Properties of Perovskite $(Pb,Ca)TiO_3$ Ceramic, *Acta Phys. Pol., A*, 2012, **122**(1), 174–179.
44 M. Ghozza, I. Yahia and S. El-Dek, Role of B-site cation on the structure, magnetic and dielectric properties of nano-sized $La_{0.7}Sr_{0.3}Fe_{1-x}M_xO_3$ (M = Mn; Co and x = 0, 0.5) perovskites, *Mater. Res. Express*, 2020, **7**(5), 056104.
45 S. Mansour, M. Karamany, R. Al-Wafi, S. El-Dek, H. A. Almossalami and M. Abdo, The effective role of diamagnetic Pb ions in tailoring the magnetic and dielectric properties of $BiFeO_3$ nanomultiferroic, *J. Mater. Sci.: Mater. Electron.*, 2021, **32**, 3621–3637.
46 M. Barsoum, *Fundamentals of ceramics*, CRC Press, 2019.
47 G. Arya, R. K. Kotnala and N. S. Negi, A novel approach to improve properties of $BiFeO_3$ nanomultiferroics, *J. Am. Ceram. Soc.*, 2014, **97**(5), 1475–1480.
48 K. L. Routray, S. Saha and D. Behera, Green synthesis approach for nano sized $CoFe_2O_4$ through aloe vera mediated sol-gel auto combustion method for high frequency devices, *Mater. Chem. Phys.*, 2019, **224**, 29–35.
49 H. P. Nguyen, G. Gyawali, Y. H. Jo, T.-H. Kim and S. W. Lee, Effect of heat treatment on ultrasonic synthesized bismuth ferrites: an effective visible light-driven photocatalyst, *Res. Chem. Intermed.*, 2017, **43**, 5113–5122.
50 D. Bilican, E. Menéndez, J. Zhang, P. Solsona, J. Fornell, E. Pellicer and J. Sort, Ferromagnetic-like behaviour in bismuth ferrite films prepared by electrodeposition and subsequent heat treatment, *RSC Adv.*, 2017, **7**(51), 32133–32138.
51 P. Mane, N. Shinde, I. Mulla, R. Koli, A. Shelke, M. Karanjkar, S. Gosavi and N. Deshpande, Bismuth ferrite thin film as an efficient electrode for photocatalytic degradation of Methylene blue dye, *Mater. Res. Express*, 2018, **6**(2), 026426.
52 X. Wang, Y. Lin, X. Ding and J. Jiang, Enhanced visible-light-response photocatalytic activity of bismuth ferrite nanoparticles, *J. Alloys Compd.*, 2011, **509**(23), 6585–6588.
53 S. P. Pattnaik, A. Behera, S. Martha, R. Acharya and K. Parida, Synthesis, photoelectrochemical properties and solar light-induced photocatalytic activity of bismuth ferrite nanoparticles, *J. Nanopart. Res.*, 2018, **20**, 1–15.
54 S. Masoudpanah, S. Mirkazemi, R. Bagheriyeh, F. Jabbari and F. Bayat, Structural, magnetic and photocatalytic characterization of $Bi_{1-x}La_xFeO_3$ nanoparticles synthesized by thermal decomposition method, *Bull. Mater. Sci.*, 2017, **40**(1), 93–100.
55 E. A. Volnistem, L. Macková, R. F. Muniz, F. R. Estrada, S. M. de Nóbrega, G. S. Dias, V. F. Freitas, L. F. Cótica and I. A. dos Santos, On the effects of dislocations on the magnetism of $BiFeO_3$ nanoparticles, *J. Alloys Compd.*, 2021, **887**, 161421.
56 M. Iqbal, A. Ali, N. A. Nahyoon, A. Majeed, R. Pothu, S. Phulpoto and K. H. Thebo, Photocatalytic degradation of organic pollutant with nanosized cadmium sulfide, *Mater. Sci. Energy Technol.*, 2019, **2**(1), 41–45.
57 A. Mehrdad, B. Massoumi and R. Hashemzadeh, Kinetic study of degradation of Rhodamine B in the presence of hydrogen peroxide and some metal oxide, *Chem. Eng. J.*, 2011, **168**(3), 1073–1078.
58 S. Ghosh, S. Roy, J. Naskar and R. K. Kole, Process optimization for biosynthesis of mono and bimetallic alloy nanoparticle catalysts for degradation of dyes in individual and ternary mixture, *Sci. Rep.*, 2020, **10**(1), 277.
59 A. Jaison, H. U. Lee, J. Hur, A. Mohan and Y.-C. Lee, Facile synthesis of Ni-doped tetrahedral γ-Bi_2O_3 and selective photocatalytic degradation of Congo red under simulated sunlight, *J. Alloys Compd.*, 2024, **1004**, 175727.
60 J. A. Nasir, S. Gul, A. Khan, Z. H. Shah, A. Ahmad, R. Khan, Z. Liu, W. Chen and D.-J. Lin, Efficient solar light driven photocatalytic degradation of Congo red dye on CdS nanostructures derived from single source precursor, *J. Nanosci. Nanotechnol.*, 2018, **18**(11), 7405–7413.
61 T. Chankhanittha, J. Watcharakitti and S. Nanan, PVP-assisted synthesis of rod-like ZnO photocatalyst for photodegradation of reactive red (RR141) and Congo red (CR) azo dyes, *J. Mater. Sci.: Mater. Electron.*, 2019, **30**, 17804–17819.

